# Understanding the role of perforations on the local hydrodynamics of gas–liquid flows through structured packings

Chemical Engineering Journal 486 (2024) 150084

Contents lists available at ScienceDirect

Chemical Engineering Journal

journal homepage: www.elsevier.com/locate/cej

# Understanding the role of perforations on the local hydrodynamics of gas–liquid flows through structured packings

Aniket S. Ambekar [a,b,*], E.A.J.F. Peters [a], Olaf Hinrichsen [b], Vivek V. Buwa [c], J.A.M. Kuipers [a]

[a] Multiphase Reactors Group, Department of Chemical Engineering and Chemistry, Eindhoven University of Technology, 5600 MB Eindhoven, the Netherlands
[b] Department of Chemistry, TUM School of Natural Sciences and Catalysis Research Center, Technical University of Munich, 85748 Garching, Germany
[c] Department of Chemical Engineering, Indian Institute of Technology Delhi, New Delhi 110016, India

ARTICLE INFO

*Keywords:*
Structure-resolved
Interface-resolved
Gas–liquid flow
Packed bed
Structured packing
Perforations

ABSTRACT

Structured packings are widely used to perform gas–liquid separation processes as they provide a large mass-transfer area and low-pressure drop. The overall performance of these packings is governed by the local liquid distribution/gas–liquid interfacial area. The local liquid distribution is substantially influenced by the arrangement and geometrical features of the structured packing. While the influence of arrangement and few geometrical features on the local liquid distribution has recently been investigated using the structure-resolved simulations, the perforations on the structured packings are usually ignored. In the present work, we have performed structure-resolved gas–liquid flow simulations, using the Volume-of-Fluid (VOF) method implemented in the open-source C++ library OpenFOAM, in a periodic domain of Mellapak.250 with and without resolving the perforations. We show that the presence of perforations results in flow separation as well as droplet formation leading to an increase in the liquid holdup, interfacial and wetted areas, irrespective of the fluid properties and wetting conditions (specified using static contact angle '$\theta_w$') considered in this work. We also show that at an inclination angle 'β' of 45° from horizontal, the location of the perforations governs the local liquid distribution and the resulting flow metrics. However, at a β of 90°, the number of perforations governs the local liquid distribution, irrespective of their location. Further, we also show that the predictions of structure-resolved VOF simulations, with perforations resolved, are in a relatively better agreement with the correlations in the literature at small values of $\theta_w$ in terms of liquid holdup and interfacial area.

## 1. Introduction

Packed beds with structured packing are commonly used to perform gas–liquid separation processes like distillation, $CO_2$ absorption from flue gases, as they provide a large mass-transfer area and low-pressure drop (see the review article by Amini and Nasr Esfahany [1]). Most of the structured packings consist of thin corrugated sheets arranged parallel to each other with contrasting channel orientations. The overall performance of these packed beds is a strong function of the local liquid distribution/gas–liquid interfacial area offered by underlying structured packing. The local liquid distribution is not only influenced by fluid properties and operating conditions, but also by the arrangement and geometrical features of structured packings. The arrangement of the structured packings is defined by the inclination angle, corrugation angle, and the minimum distance between two consecutive sheets. Whereas, the geometrical features of individual sheets include height, base, and crimping angle of the corrugations as well as perforations, and surface textures (please see Fig. 1 for the definition of these parameters). Therefore, structure-resolved measurements and simulations play a crucial role in not only understanding the local gas–liquid hydrodynamics, but also in the development of improved structured packings.

Structure-resolved measurements of liquid distribution can be performed using non-invasive tomographic techniques like gamma-ray tomography, X-ray tomography, Ultrafast X-ray tomography, and X-ray microtomography. However, these tomographic techniques either have limited spatial and/or temporal resolution and are expensive (see articles by Schubert et al. [2], Bradtmöller et al. [3], Schug and Arlt [4], Flechsig et al. [5] for details). With the increasing affordability of computational resources, interface-resolved simulations of gas–liquid flow through structure-resolved domains using interface-capturing methods like Volume-of-Fluid (VOF), Level Set, etc. are gaining popularity. Recently, a few researchers validated the predictions of structure-

* Corresponding author.
*E-mail addresses:* a.s.ambekar@tue.nl, aniketambekar.iitd@gmail.com (A.S. Ambekar).

https://doi.org/10.1016/j.cej.2024.150084

Available online 2 March 2024

resolved VOF simulations with the aid of measurements of liquid spreading over smooth inclined plate [6–8]. For example, Haroun et al. [6] and Olenberg and Kenig [7], reported a good agreement in predictions of gas–liquid interface morphology and wetted area compared to the measurements by Hoffmann et al. [8] for a wide range of liquid Reynolds number. Bertling et al. [9], reported a good agreement between the predictions and the corresponding measurements (performed by Lan et al. [10]) in terms of local liquid film thickness. Structure-resolved VOF simulations are also shown to predict the gas–liquid interface morphology of liquid spreading over an inclined wavy plate for a wide range of liquid Reynolds number [11]. Bertling et al. [9], also performed measurements as well as VOF simulations of liquid spreading on textured (L-grooved and W-grooved) inclined sheets and showed that the structure-resolved VOF simulations can predict the gas–liquid interface morphology and local liquid film thickness by considering an appropriate three-phase static contact angle instead of resolving the textures.

Concerning structured packings, several researchers have validated the macroscopic predictions (in terms of liquid hold-up, interfacial area, and pressure drop) of structure-resolved VOF simulations with bed-scale measurements and semi-empirical correlations, derived from bed-scale measurements. For example, Singh et al. [12], reported a satisfactory agreement in the measured and predicted liquid holdup for Schwarz-D packing for liquid loads below 50 $m^3/m^2hr$. Similarly, Macfarlan et al. [13], reported a reasonable agreement in predicted and measured (performed by Green et al. [14]) liquid holdup of Mellapak.250Y packing. Whereas, Singh et al. [12], Gu et al. [15], Olenberg and Kenig [7], Yang et al. [16], and Sebastia-Saez et al. [17], reported a reasonable agreement in the predicted liquid holdup, interfacial area as well as pressure drop with that estimated from correlations by Sues et al. [18], Olujic et al. [19,20], Billet and Schultes [21], Stichlmair [22], Mackowaik [23], etc. Further, the qualitative comparison of the measured and predicted gas–liquid interface morphology of liquid spreading over structured packing reveals a satisfactory agreement in the measurements and predictions of structure-resolved VOF simulations [24,25].

The validated structure-resolved VOF simulations are further used to investigate various flow regimes of liquid spreading over smooth inclined plate, wavy plate as well as corrugated sheets. It is shown that the liquid spreading over an inclined plate is characterized by droplet formation at Weber (We) number (defined based on the superficial liquid velocity and liquid film thickness) values $\ll 1$. Whereas the intermediate values of the We number, i.e. $< 1$, result in rivulet formation. Further increase in the We value to approximately 1 leads to channeling followed by full film flow at We $> 1$ (see Iso et al. [11], and Haroun et al. [6]). Similar flow regimes were also observed for liquid spreading over a wavy plate, however, transitions between regimes occurred at lower values of We as compared to the flow over an inclined plate [11]. With respect to corrugated sheets, droplet formation was observed at small liquid loads ($U_L$) and large three-phase static contact angle '$\theta_w$' (approaching 90°). Rivulets were formed at an intermediate $U_L$ and large $\theta_w$, whereas the film flow was observed at large $U_L$ and small $\theta_w$ (see Haroun et al. [6], Singh et al. [24], Olenberg and Kenig [7], and Sebastia-Saez et al. [17] for further details).

Recently, a few researchers have also investigated the effect of arrangement on the void-scale hydrodynamics through a representative elementary unit (REU) of structured packing using the VOF simulations [7,15,26]. These investigations report that the corrugation angle of 45° is associated with the maximum interfacial and wetted area. These structure-resolved simulations also reveal that the smaller the minimum distance between two consecutive corrugated sheets, the better the performance in terms of interfacial and wetted area. The effects of fluid properties, gas/liquid flow rates, and surface wettability (through static and dynamic three-phase contact angle models), on the macroscopic hydrodynamic performance parameters, as well as void-scale liquid spreading, were also investigated using the structure-resolved VOF simulations [6,7,12,16,17,24,26,27]. Singh et al. [27] performed structure-resolved VOF simulations of liquid flowing over an inclined smooth plate as well as a corrugated sheet by implementing both static and dynamic contact angle models. Their investigation revealed that the influence of dynamic contact angle, for corrugated sheet, on the predictions of gas–liquid interfacial area is marginal. Further, the void-scale dynamics through the REU of differently structured packings like Mellapak, Montz, Gempak, etc., representing specific geometrical features were also investigated using structure-resolved VOF simulations [27–30]. Further, Raynal et al. [28] and Fernandes et al. [29] utilized the predictions of structure-resolved VOF simulations to propose a methodology to estimate wet pressure drop using single-phase *meso*-scale simulations. The structure-resolved VOF simulations were also used to propose novel XW-pack which resulted in better local liquid distribution as compared to Rombopak9M-3D with similar surface area per unit volume by Sarajlic et al. [30]. Moreover, structure-resolved VOF simulations were also used to modify the existing semi-empirical correlations as well as to propose new correlations to estimate macroscopic performance parameters of structured packings [24,25,31].

In all the above investigations, the surface textures are not resolved but considered through the apparent three-phase static contact angle.

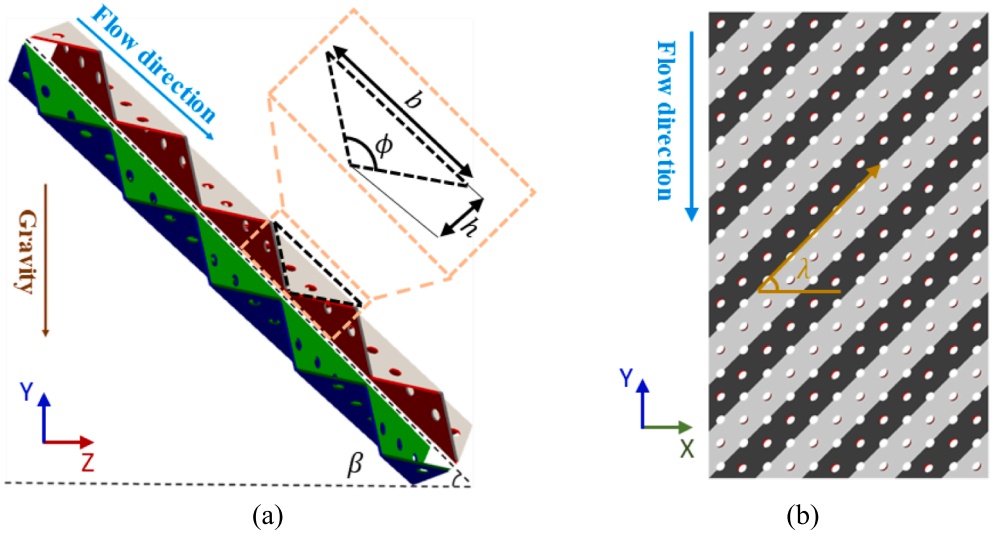


**Fig. 1.** Schematics of structured packing's (a) Y-Z, and (b) X-Y view displaying the arrangement as well as geometrical features.

This is reasonable because of the substantially different length-scales of the surface textures (a few microns) and other geometrical features (a few millimeters) of the sheets. However, all of the above studies also completely ignored the millimeter-sized perforations. Two reasons are cited for this, namely, 1) the requirement of large computational resources in spatially resolving perforations and 2) the assumption of liquid-phase flowing over the perforation without passing through it (based on the X-ray tomography measurement performed by Green et al. [14]). Therefore, the specific contributions of the perforations to the local hydrodynamics of the structured packing are not understood. In view of this, the objectives of the present work are a) to perform structure-resolved VOF simulations of gas–liquid flows through Mellapak.250 packing with and without perforations, b) to investigate the effect of perforations and their location on the local hydrodynamics as a function of inclination angle ($\beta$), and c) to study the effect of perforations on the local liquid distribution as a function of liquid load and surface wettability.

## 2. Methodology

### 2.1. Creation of structure-resolved domain and computational mesh

The geometry for a corrugated sheet with a corrugation base ($b$) of 26.7 mm and height ($h$) of 12 mm with crimping angle ($\phi$) of 96° corresponding to Mellapak.250 (*https://www.sulzer.com*) was created using the commercial software SpaceClaim v19.2 (see Fig. 1 for the definitions of aforementioned parameters). The corrugation angle ($\lambda$) of 45° was considered as it provides the maximum gas–liquid interfacial area [7,15,26]. Two sheets were placed parallel to each other with contrasting channel orientations such that the minimum distance between them is 2 mm (as considered in the literature [16,24,27]). A single periodic repeating unit of the abovementioned arrangement was identified. The periodic repeating unit was multiplied 3 times in the lateral direction (X-axis) and 5 times in the vertical direction (Y-axis) to create a representative domain. The volume between the two parallel sheets was considered as the computational domain to simulate two-phase flow through structured packing without perforations. This resulted in a fluid domain with maximum extents of 113.85 mm × 189.75 mm × 26 mm, periodic in two directions i.e. X and Z [see Fig. 2 (a)]. Further, circular perforations with a diameter ($d$) of 4 mm, similar to Sulzer Mellapak perforated sheet, and a inter-perforation distance of 12 mm were created on the corrugated sheets. To avoid difficulties in meshing, the sheets were considered to be 1 mm thick. In reality, the corrugated sheets are substantially thinner. This perforated sheet geometry was subtracted from the box with dimensions 113.85 × 189.75 × 30 $mm^3$ and resulted in a computational domain periodic in all directions [see Fig. 2 (b)]. The perforations were positioned on the sides, ridges, and on both sides as well as ridges as shown in Fig. 3 (a), (b), and (c), respectively, to investigate the role of perforation location on the local hydrodynamics. It should be noted that the presence of perforations on either the side or ridge results in a decrease in the area of the corrugated sheet by 5 % as compared to the non-perforated sheet. This also means that the presences of perforations on both side and ridge results in the area of corrugated sheet to be reduced by 10 %.

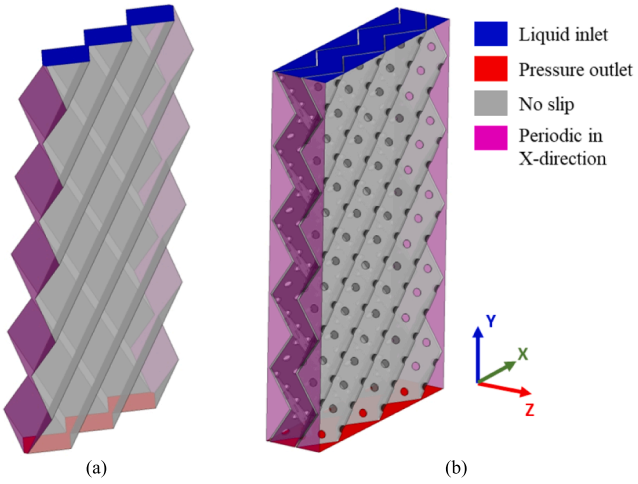


**Fig. 2.** Computational domain (a) without and (b) with perforations resolved along with boundary conditions. *Note: The domain in Fig. 2 (b) is also periodic in Z-direction. For the ease of visualization the faces periodic in Z-direction are rendered transparent.*

In order to create the computational mesh for the fluid domains, initially, the surfaces of the sheets were spatially discretized with triangular elements using commercial software Fluent v19.2. The size of the triangular elements was specified to be $d/16$, $d/32$, and $d/64$ to create a surface mesh with coarse, medium, and fine resolution, respectively. The generated triangular elements were transformed to hexagonal elements and polyhedral cells were created on the top of these hexagonal elements [see Supplementary Fig. S1 (a) for surface mesh of corrugated sheet with coarse resolution]. The cells were allowed to grow by a factor of 1.2 away from the sheet surfaces with maximum cell size limited to $d/8$. This resulted in grids with 0.3, 1.8, and 6 million cells for coarse, medium, and fine resolution, respectively for fluid domains without perforations. As will be briefly discussed in Section 3, and more extensively in the Supplementary material, the medium grid resolution was found sufficient, in terms of all examined flow metrics i.e. liquid holdup, interfacial area, wetted area, and pressure drop, to investigate two-phase flow through the non-perforated sheet geometry. Therefore, the medium grid resolution was used as the base to spatially discretize the fluid domains with perforations resolved. The edges representing perforations were specified with element size of $d/32$, $d/64$, and $d/96$ resulting in grids with element counts of 3, 3.7, and 4.3 million, respectively, for the domain with perforations on the side. Please see Supplementary Fig. S1 (b) for surface mesh of corrugated sheet with perforations.

### 2.2. Computational model

In the present work, the structure-resolved Volume-of-Fluid (VOF) simulations of liquid [density ($\rho_l$): 1000 kg/$m^3$ and dynamic viscosity ($\mu_l$): 1 × $10^{-3}$ Pa•s] following through the small sections of structured packing, initially, occupied with gas [density ($\rho_g$): 1 kg/$m^3$ and dynamic viscosity ($\mu_g$) of 1.48 × $10^{-5}$ Pa•s] are performed using open-source flow solver code OpenFOAM v6. The flow is considered laminar, and the fluids are considered Newtonian as well as incompressible.

#### 2.2.1. Governing equations

In the VOF method [32], a single set of continuity [Eq. (1)] and momentum [Eq. (2)] equations, as given below is solved,

$$\nabla \bullet \vec{v} = 0 \tag{1}$$

$$\frac{\partial}{\partial t}(\rho \vec{v}) + \nabla \bullet (\rho \vec{v}\vec{v}) = -\nabla p + \rho \vec{g} + \nabla \bullet \left[\mu\left(\nabla \vec{v} + (\nabla \vec{v})^T\right)\right] + \vec{F_S} \tag{2}$$

where $\vec{v}$ is the velocity (m/s), $p$ is the pressure (Pa), $\vec{g}$ is the acceleration due to gravity (m/$s^2$), and $\vec{F_S}$ is the surface tension force per unit volume (N/$m^3$). $\rho$ and $\mu$ are the phase volume fraction weighted density (kg/$m^3$) and viscosity (Pa•s) and are computed as follows,

$$\rho = \alpha_l \rho_l + (1 - \alpha_l)\rho_l \tag{3}$$

$$\mu = \alpha_l \mu_l + (1 - \alpha_l)\mu_l \tag{4}$$

where, $\alpha_l$ and $\alpha_g$ ( $= 1 - \alpha_l$) are the volume fractions of liquid- and gas-

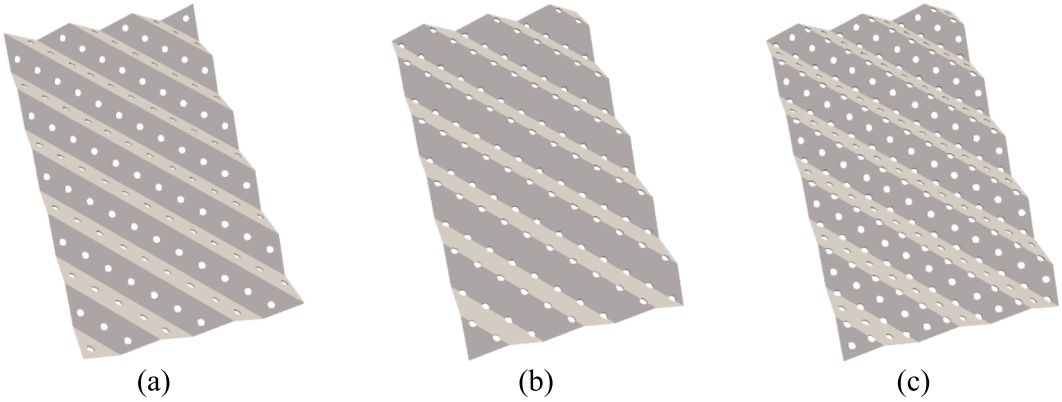


**Fig. 3.** Corrugated sheet geometry with perforations on (a) side, (b) ridge, and (c) both on ridge and side.

phase, respectively.

The motion of the gas–liquid interface is simulated by solving the advection equation [Eq. (5)] for $\alpha_l$,

$$\frac{\partial}{\partial t}(\alpha_l \rho_l) + \nabla \bullet (\alpha_l \rho_l \vec{v}) + \nabla \bullet \left(\alpha_l (1-\alpha_l) \vec{u}_r\right) = 0 \tag{5}$$

where, $\vec{u}_r$ is compression velocity and the third term in the left-hand side of Eq. (5) represents artificial compression used to limit numerical diffusion (see [33] for details). The $\alpha_l$ fluxes are corrected to ensure boundedness and conservativeness using the Multidimensional Universal Limiter with Explicit Solution (MULES) algorithm (see [34] for details).

The $\vec{F_s}$ is computed using the Continuum Surface Force model (proposed in [35]), given as,

$$\vec{F}_S = -\gamma \kappa \nabla \alpha_l \tag{6}$$

where $\gamma$ is the gas–liquid surface tension (72 mN/m), $\kappa$ is the local curvature of the gas–liquid interface, and is calculated using the local gradients of the surface normal ($\hat{n}$) of the interface as shown below,

$$\kappa = \nabla \bullet \hat{n} \tag{7}$$

$$\hat{n} = \nabla \alpha_l / |\nabla \alpha_l|$$

The wettability of the sheet surfaces was modelled using the wall adhesion by specifying the static contact angle ($\theta_w$) as,

$$\hat{n} = \hat{n}_w \cos\theta_w + \hat{t}_w \sin\theta_w \tag{8}$$

where $\hat{n_w}$ and $\hat{t_w}$ are the unit vectors normal and tangential to the cell faces on the sheet surfaces, respectively.

### 2.2.2. Initial, boundary conditions, and numerics

The structure-resolved fluid domains were initialized with $\alpha_l = 0$ (i.e. filled with gas at t = 0). A constant inlet velocity of $8.6 \times 10^{-3}$, $1.72 \times 10^{-2}$, and $3.15 \times 10^{-2}$ m/s along with $\alpha_l = 1$ is specified at the liquid inlet located at the top (see Fig. 2) resulting in liquid load $U_l$ of 31, 62, and 110 $m^3/m^2hr$, respectively. A constant pressure (101.325 kPa) boundary condition is applied at the outlet, with backflow $\alpha_l$ set to 0 allowing liquid to exit the domain. A no-slip boundary condition along with a $\theta_w$ of 30, 50, and 70° is specified on the sheet surfaces to investigate the role of varying wettability on the void-scale hydrodynamics. The cell faces representing perforations are also specified with no-slip boundary condition along with $\theta_w = 70°$. All other domain boundaries are assigned periodic boundary condition (see Fig. 2).

Transient VOF simulations were performed by using a variable time step '$\Delta t$' [Eq. (9)] that satisfied both the capillarity [Eq. (10)] [35] and Courant–Friedrichs–Lewy [Eq. (10)] criterion,

$$\Delta t = MIN(\Delta t_c, \Delta t_{CFL}) \tag{9}$$

$$\Delta t_c \leq \sqrt{\frac{\rho_{avg} \Delta x_{min}^3}{2\pi\gamma}} \tag{10}$$

$$1 \leq \frac{\Delta t_{CFL} \vec{v}}{\Delta x_{min}} \tag{11}$$

to ensure the stability of the Continuum Surface Force model [Eq. (6)], here $\Delta x_{min}$ is the smallest element size and $\rho_{avg} = (\rho_l + \rho_g)/2$. This resulted in $\Delta t$ values between $5 \times 10^{-6}$ and $5 \times 10^{-5}$ s. The Pressure-Implicit with the Splitting of Operators (PISO) scheme was used for pressure–velocity coupling. Second-order numerical schemes were used to discretize the spatial derivatives in Eqs. (1), (2), and (5), while the first-order Euler scheme was used to discretize temporal derivatives in the these equations. The convergence criterion for all the variables was set to a residual of $1 \times 10^{-6}$ other than that for $\alpha_l$ which was specified to a residual of $1 \times 10^{-10}$.

## 3. Results and discussion

As mentioned in Section 2.1, three grids, namely, Coarse, Medium, and Fine with grid resolution of 0.3, 1.8, and 6 million elements, were created for the fluid domain without perforations to investigate the effect of grid resolution on the predictions of VOF simulations. Supplementary Figs. S2 (a), (b), (c), and (d) compares the predictions of the time-evolution of liquid holdup 'LH' (calculated as the volume fraction of fluid domain occupied by liquid), interfacial area 'IA' (determined as the area of the *iso*-surface with $\alpha_l = 0.5$ and normalized by the area of corrugated sheets), wetting efficiency 'WE' (defined as the area-fraction of corrugated sheets occupied by liquid), and pressure drop '$\Delta P$', respectively as function of grid resolution. From the results it is evident that the Coarse grid underpredicts all flow metrics other than $\Delta P$. Whereas the differences in the predictions of all the parameters predicted by the Medium and Fine grid are marginal. Therefore, the medium grid resolution is used for all the subsequent simulations. The medium grid resolution was also considered as the base to spatially discretize fluid domains with perforations. The circular edges representing perforations were refined resulting in grids with element count 3, 3.7, and 4.3 million for the fluid domain with perforations on the side (see Section 2.1 for details) to establish the grid resolution required to resolve perforations. Supplementary Fig. S3 reveals a negligible deviation in predictions of LH, IA, WE, and $\Delta P$ as a function of grid resolution. However, Supplementary Fig. S3(e) shows that the grid with element count of 3.7 million elements is required to reasonably predict the time-evolution of area-fraction of perforations occupied by the liquid-phase. Therefore, the specifications of grid with 3.7 million elements are used

to create grids for fluid domains with perforations, irrespective of their location, in all the subsequent simulations.

### 3.1. Effect of perforation location

Perforations with d = 4 mm and inter-perforation distance of 12 mm were created on the side, ridge, and on both side and ridge of the corrugated sheets (see Fig. 3) to investigate the effect of perforation location on the local hydrodynamics and the resulting flow metrics. Furthermore, the inclination angles ($\beta$) of 45 and 90° were taken into consideration to explore their influence on different perforation locations (see Fig. 4 to visualize the definition of $\beta$). The liquid load '$U_l$' and $\theta_w$ was specified to be 62 $m^3/m^2hr$ and 70°, respectively.

#### 3.1.1. Inclination angle of 45°

At a $\beta$ of 45°, it is observed that the presence of perforations on the side results in an increase in the IA and wetted area 'WA' with marginal difference in liquid holdup as compared to the case without perforations [see Fig. 5(a)–(c) and Table 1]. The change in perforation location from side to ridge results in a substantial increase in LH, IA, and WA. However, the presence of perforations on both side and ridge leads to LH, IA, and WA similar to the case with perforations on the ridge [see Fig. 5(a), (b) and (c), respectively and Table 1]. It should be noted that the presence of perforations on either the side or ridge results in a decrease in the area of the corrugated sheet by 5 % as compared to the non-perforated sheet. This also means that the presences of perforations on both side and ridge results in the area of corrugated sheet to be reduced by 10 %. Therefore, for the ease of visualization, the surface area of non-perforated sheets is used to normalize both wetted and interfacial area instead of using the case-specific surface area of the sheets. Further, it is also observed that the time-averaged $\Delta P$ is not influenced by the presence of perforations, irrespective of their locations [see Fig. 5(d) and Table 1]. However, the amplitude of pressure fluctuations is large in the presence of perforations, especially in the case of perforations on the ridge. To understand the aforementioned trends in LH, WA, IA, and $\Delta P$ as a function of perforation location, the local hydrodynamics was analyzed and quantified in terms of the WA of each side of the individual sheets and the number of wetted perforations specific to each individual sheet. Please, see Fig. 4 for the location and identity of each side of the corrugated sheets.

In the case of no perforations, the liquid flows through the channels provided by the corrugated Sheet 1 without wetting Sheet 2 [see Fig. 6 (a)]. Such a flow behavior is observed because at a $U_l$ of 62 $m^3/m^2hr$, the liquid is unable to reach the proximity regions i.e. the regions with minimum distance between two consecutive sheets. These proximity regions are known to increase the fluid–solid interaction by changing the local flow direction. On the other hand, the presences of perforations on the sides results in the liquid-phase flowing from one side to the other side of the corrugated sheet through the perforations [see Fig. 6(b)]. However, very few perforations [≅ 10 % as shown in Fig. 7(a)], which are located near the inlet, interact with the liquid-phase. Therefore, the flow behavior on the top side of Sheet 1 is like the channel flow observed on the non-perforated Sheet 1 [see Fig. 6(a) (i) and (b) (i)]. The interaction of the liquid-phase with the perforations is also associated with large values of shear stress [see Supplementary Figs. S4(b) and (e)] leading to flow separation and flow of small liquid streams on the other side of the sheet i.e. on the bottom side of Sheet 1. The fluctuations in $\Delta P$ are also a signature of flow separation events. These small liquid streams flow over the surface of corrugated sheet eventually break to form small droplets due to the gravity driven nature of the flow [see Fig. 5(b) (ii)]. This flow behavior results in small decrease in the WA of the top side of Sheet 1 as well as a significant increase in the WA of the bottom side of Sheet 1 [see Fig. 8(a) and (b)]. Similar flow behavior and values of WA are observed for the corresponding sides of Sheet 2 due to periodicity boundary conditions and are not shown to avoid repeatability. Such a flow behavior also results in an increase in IA and overall WA with marginal influence on the LH as compared to the domain without perforations [see Fig. 5(a)–(c)].

When the perforation location is changed from side to ridge, approximately half of the perforations interact with the liquid as it primarily flows through the channels formed by the corrugated sheets [see Figs. 6(c) (i) and 7 (a) (ii)]. As mentioned earlier, the presence of perforations leads to flow separation as it is associated with substantially large values of wall shear stress [see Supplementary Figs. S4 (c) and (e)]. Since the flow separation events increase with the change in perforation location from side to ridge, the amplitudes of fluctuations in $\Delta P$ also increase [see Fig. 5(d)]. However, unlike formation of droplets on the bottom side of Sheet 1, in the case of perforations on the side, the small streams of liquid [Fig. 6(b) (ii)], formed due the interaction of the liquid and the perforations, merge to form a single stream of liquid flowing over the surface of the corrugated sheet [Fig. 6(c) (ii)]. These merged streams of liquid flowing on the bottom side of Sheet 1 eventually interact with the consecutive sheet in the proximity region resulting in droplet formation as is evident on the near-outlet region of the top side of Sheet 1 [see Fig. 6(c) (i)]. Interestingly, the liquid flows from the top to the bottom side of Sheet 1 through the perforations on the ridge such

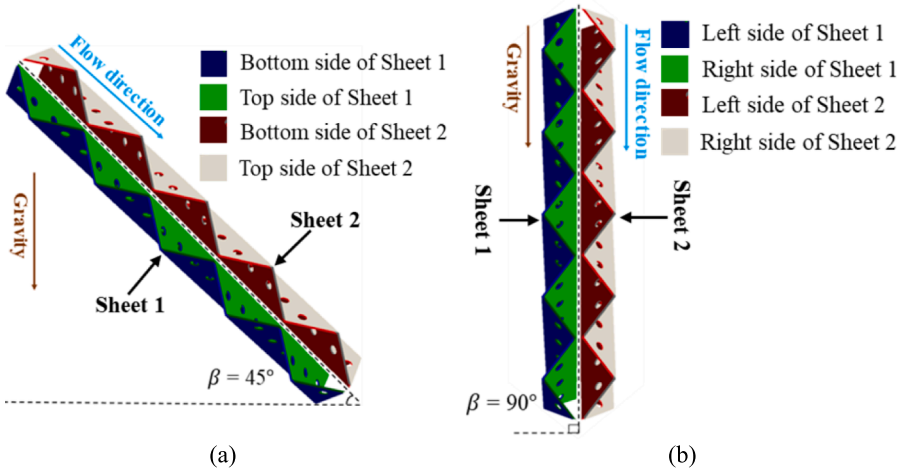


**Fig. 4.** Schematic of corrugated sheets at a $\beta$ of (a) 45 and (b) 90° illustrating the identity of different regions. *Note: At a $\beta$ of 45°, the flow behavior on the Bottom and Top side of Sheet 1 is similar to the flow behavior on the Bottom and Top side of Sheet 2, respectively (discussed later in Section 3.1). Therefore, flow behavior on the Bottom and Top side of Sheet 1 is shown and described in later Figures. Further, at a $\beta$ of 90°, the flow behavior on all the sides, irrespective of the sheet is identical (discussed later in Section 3.2). Hence, the flow behavior on the Right side of Sheet 1 is shown and described as a representative of all the sides of Sheet 1 and 2.*

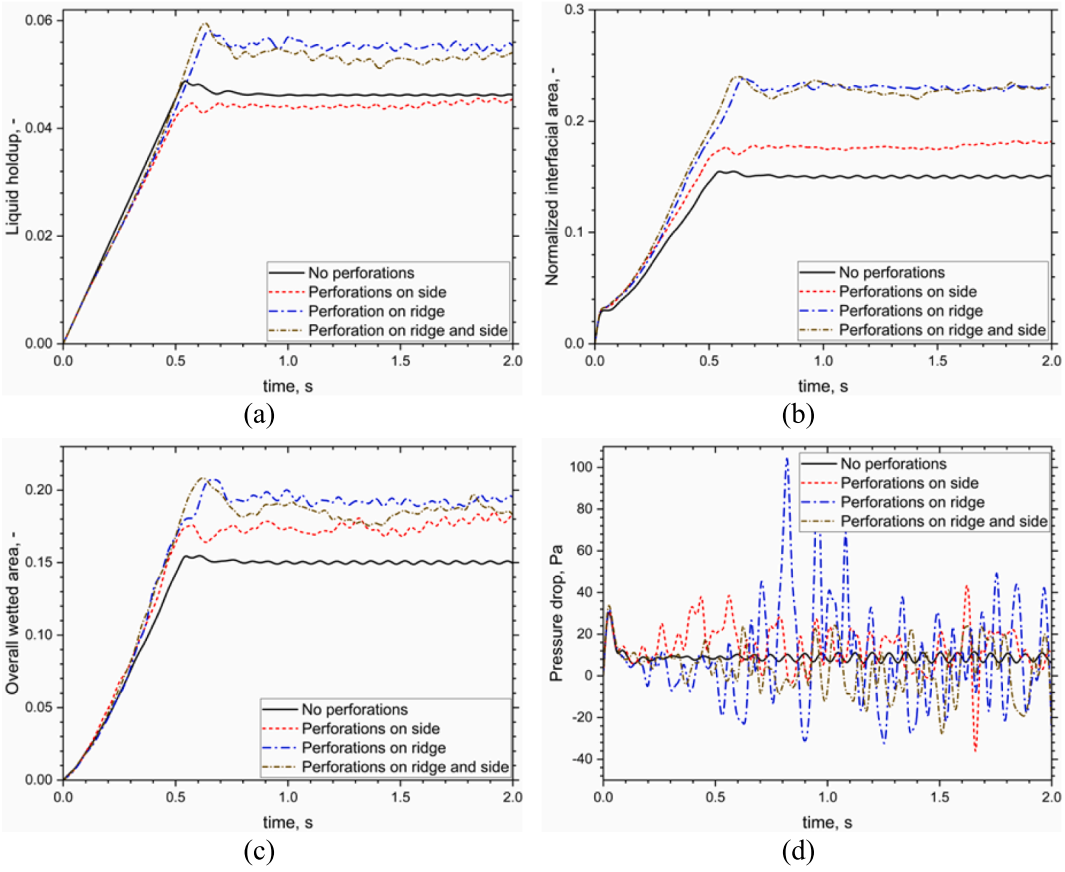


**Fig. 5.** Effect of perforation location on (a) liquid holdup, (b) interfacial area, (c) wetted area and (d) pressure drop ($\beta = 45°$, $\theta_w = 70°$, $U_l = 62$ m$^3$/m$^2$hr).

**Table 1**
Predictions of time-averaged flow metrics as a function of perforation location and inclination angle ($U_l = 62$ m$^3$/m$^2$hr, $\theta_w = 70°$). *Note: The time-averaging was performed until the residual of time-averaged LH, IA, Overall WA, as well as ΔP was below ± 1 × 10$^{-4}$ and required ≅ 1 s of flow time. The initial transients* i.e. *information up to t = 1 s, were not considered for time-averaging.*

| $\beta$,° | Perforation location | LH, - | IA, - | Overall WA, - | $\Delta P$, Pa |
|---|---|---|---|---|---|
| 45 | – | 0.046 | 0.15 | 0.15 | 8.695 |
| | Side | 0.044 | 0.177 | 0.175 | 8.639 |
| | Ridge | 0.055 | 0.23 | 0.192 | 9.75 |
| | Side and ridge | 0.053 | 0.228 | 0.185 | 9.013 |
| 90 | – | 0.045 | 0.233 | 0.162 | −14.598 |
| | Side | 0.049 | 0.284 | 0.172 | −13.728 |
| | Ridge | 0.048 | 0.298 | 0.169 | −13.145 |
| | Side and ridge | 0.053 | 0.339 | 0.179 | −11.437 |

that after an approximately half the channel length the liquid no longer follows the channel on the top side of Sheet 1. Such a flow behavior results in a decrease in WA of the top side of Sheet 1 and a substantial increase in the WA of the bottom side of Sheet 1 leading to a substantial increase in LH, IA, and overall WA relative to the case with perforations on the side [see Fig. 5(a)–(c)].

In the case with perforations located on both side and ridge, the flow behavior is very similar to the case with perforations on the ridge. However, it is also associated with a few perforations on the side, near the inlet, interacting with the liquid-phase [see Figs. 6(d) and 7 (c)]. This leads to a decrease in the extent of channel flow on the top side of the bottom sheet relative to the extent of channel flow in the case of perforations on the ridge [Fig. 6(d) (i)]. This also results in smaller number of perforations interacting with liquid-phase relative to the perforations on the ridge [Fig. 7(a)–(b)] and is therefore, associated with smaller wall shear stress as well as smaller amplitude of fluctuations in $\Delta P$ as compared to the case with perforations on ridge [Supplementary Figs. S4 (e) and 5 (d)]. Such a flow behavior leads to more liquid flowing on the bottom side as compared to the top side of Sheet 1 [see Fig. 8(a) and (b)]. However, the change in flow behavior does not influence the LH, IA, and overall WA as the majority of liquid interacts with the perforations located on the ridge. In summary, at a $\beta$ of 45°, the location of perforation plays a significant role in deciding the flow path as well as flow behavior and the appropriate location of perforation can substantially enhance the flow metrics of corrugated sheets.

### 3.1.2. *Inclination angle of 90°*

At a $\beta$ of 90°, rivulets are formed near the inlet on each side of the corrugated sheets irrespective of the perforation location unlike the channel flow observed at a $\beta$ of 45° [see Fig. 9(a)–(d)]. In the case of no perforations, these rivulets separate in two liquid streams as the rivulet interacts with the consecutive sheet in the proximity regions [see Fig. 9 (a) and Supplementary Video V1]. The newly formed liquid streams flow in different directions i.e. one along the flow direction and the other along the corrugation angle. Further, these liquid streams break to form droplets due to their interactions with the proximity regions and due to the increased magnitude of the component of gravitational force along the flow direction at a $\beta$ of 90° relative to that at a $\beta$ of 45°. The flow separation at the proximity region leading to two liquid streams flowing in different direction is also reported by Olenberg and Kenig [7] at similar flow conditions. However, Olenberg and Kenig [7] did not observe droplet formation as the considered domain size was significantly small i.e. single repeating periodic element. The increased magnitude of the gravitational force is evident from the decrease in $\Delta P$ to a negative value [see Fig. 5(d) and 10(d)]. A similar flow behavior is observed on the other corrugated sheet [see Fig. 9(a) and Supplementary

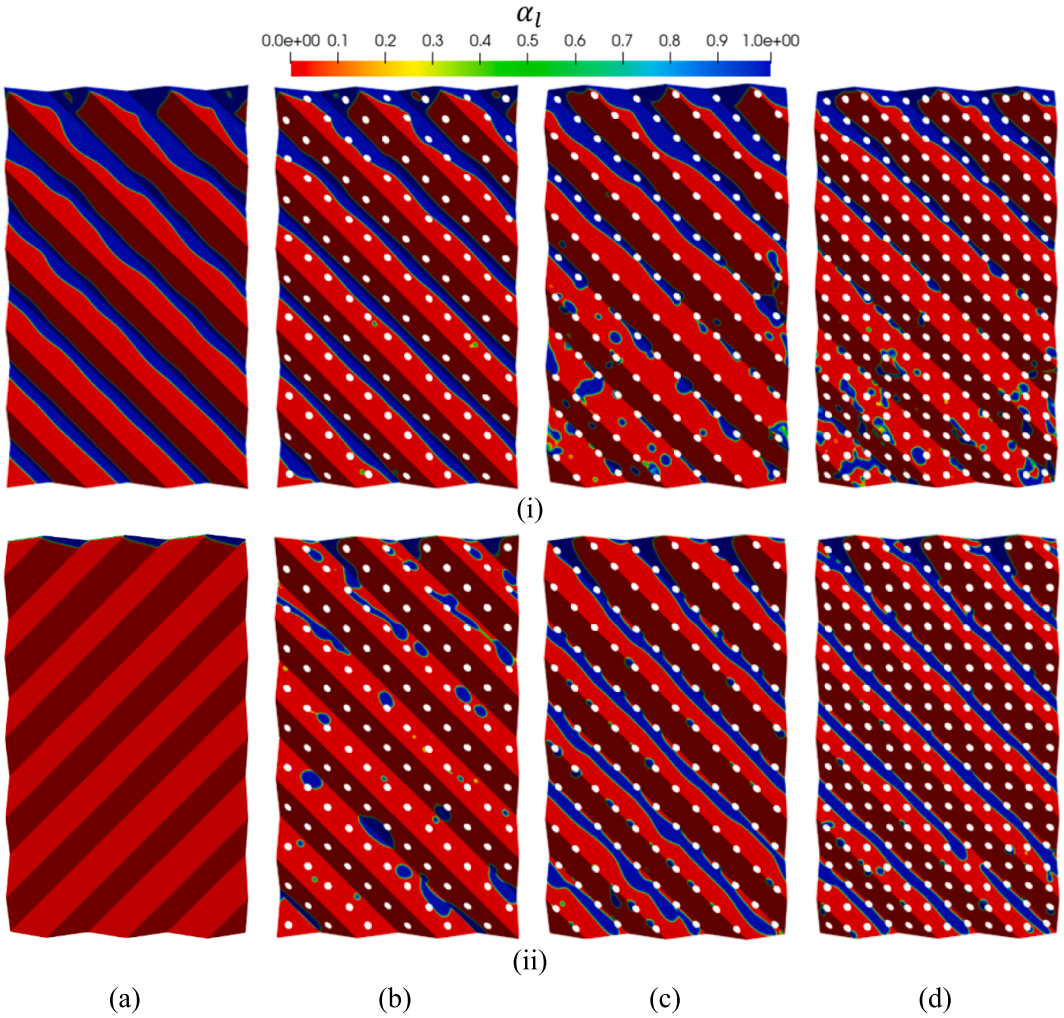


**Fig. 6.** Instantaneous local liquid distribution on the (i) top and (ii) bottom side of Sheet 1 (a) without perforations as well as with perforations on (b) side, (c) ridge, and (d) on both side and ridge at t = 3 s ($\beta = 45^{\circ}$, $\theta_w = 70^{\circ}$, $U_l = 62$ m$^3$/m$^2$hr).

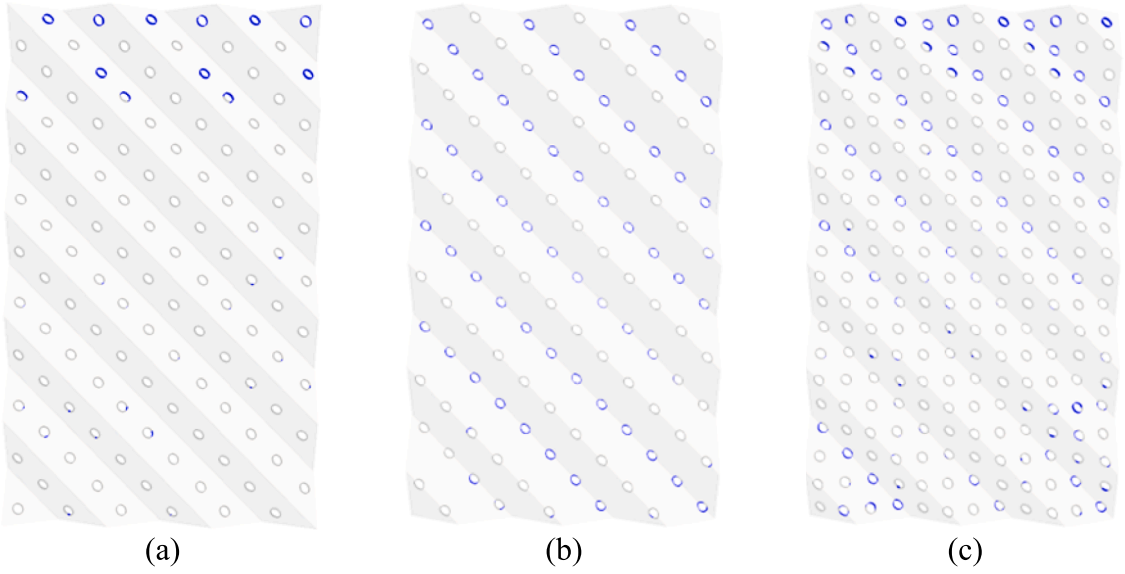


**Fig. 7.** Visualization of the perforations on Sheet 1 interacting with the liquid-phase as a function of their location i.e., on (a) side, (b) ridge, as well as (c) both side and ridge. *Note: In Fig. (a)-(b), the blue color represents perforation-surface faces with value of time-averaged $\alpha_l \geq 0.1$. The time-averaging was performed for 1 s of flow time after pseudo-steady state was achieved* i.e. *after 2 s.* (For interpretation of the references to color in this figure legend, the reader is referred to the web version of this article.)

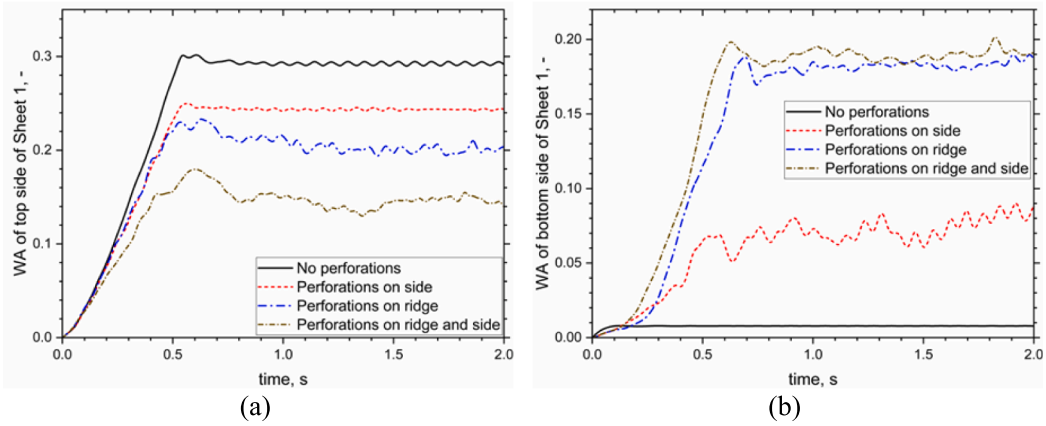


**Fig. 8.** Effect of perforation location on the wetted area of the (b) top, and (c) bottom side of Sheet 1 ($\beta = 45°$, $\theta_w = 70°$, $U_l = 62$ m$^3$/m$^2$hr).

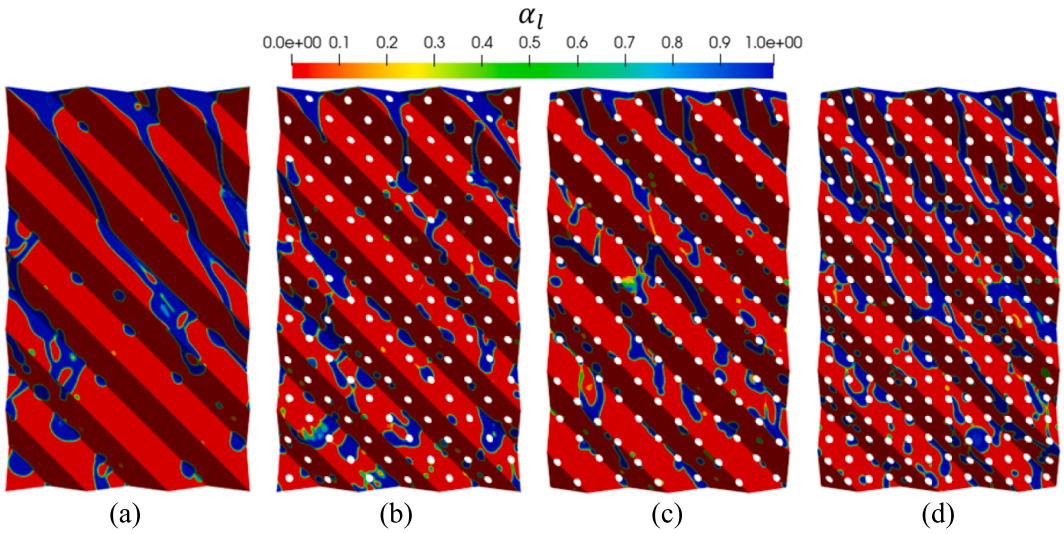


**Fig. 9.** Instantaneous local liquid distribution on the right of Sheet 1 (a) without perforations as well as with perforations on (b) side, (c) ridge, and (d) on both side and ridge at t = 3 s. Also see Supplementary Videos for the time-evolution of liquid distribution on the right side of Sheet 1 (V1) without perforations as well as with perforations on (V2) side, (V3) ridge, and (V4) both side and ridge ($\beta = 90°$, $\theta_w = 70°$, $U_l = 62$ m$^3$/m$^2$hr). *Note: All the supplementary videos are 50 times slower for the ease of visualization.*

Fig. S5 (a)] unlike that at a $\beta$ of 45° where the liquid never contacts Sheet 2. The similar flow behavior on both the sheets is also evident from the similar time-evolution of WA on these sheets [Supplementary Figs. S6 (b)–(c)]. Such a flow behavior results in a substantial increase in IA with marginal change in LH, and overall WA as compared to that at a $\beta$ of 45° [see Figs. 5 and 10].

Further, the presences of perforations on either side or ridge results in an increase in LH, IA, and overall WA as compared to that of without perforations [Fig. 10(a)–(c)]. Interestingly, the presence of perforations on either side or ridge also results in a similar flow metrics, in terms of LH, IA, overall WA, and $\Delta P$. This is observed because all the perforations interact with the liquid-phase, irrespective of their location leading to droplet formation from the very beginning [see Supplementary Figs. S6 (a) (i)–(ii), S5(b)–(c), Fig. 9(b)–(c), and Supplementary Videos V2–V3]. Unlike at a $\beta$ of 45°, where the liquid only flows from the top to the bottom side of Sheet 1 through perforations (see Supplementary Fig. S7), at a $\beta$ of 90°, the liquid flows from the right to the left side of a sheet and vice versa. A single liquid stream or droplet enters from one side of the sheet to the other side through a perforation and re-enters to the side of origin through another perforation as shown in Supplementary Fig. S8. Such flow paths lead to an increased interaction between the liquid and the corrugated sheet resulting in the observed substantial increase in IA [Fig. 10(b)] with marginal change in LH and overall WA [Fig. 10(a) and (c)]. The presences of perforations on both side and ridge result in twice the number of perforations relative to the number of perforations located on either side or ridge. Further, all these perforations interact with the liquid-phase [Supplementary Fig. S6(a) (iii) and Video V4] resulting in a proportionate increase in the LH, IA, and overall WA [Fig. 10(a)–(c)]. Therefore, at a $\beta$ of 90° the number of perforations decides the flow metrics irrespective of the perforation location. However, it should be noted that the increase in the perforation number is also associated with the increase in the wall shear stress [Supplementary Fig. S9] which results in the erosion of the sheets. Since the $\beta$ of 90° and perforations located on both side and ridge results in the largest IA, these specifications are considered to investigate the effect of liquid load and surface wettability on the local hydrodynamic and flow metrics of corrugated sheets.

### 3.2. *Effect of liquid load*

In this section, we discuss the effect of liquid load on the hydrodynamic performance of structured packing with and without perforations resolved. Three values of $U_l$ i.e. 31, 62, and 110 m$^3$/m$^2$hr at a $\beta$ of 90° and a $\theta_w$ of 70° are considered. As is evident from the Supplementary

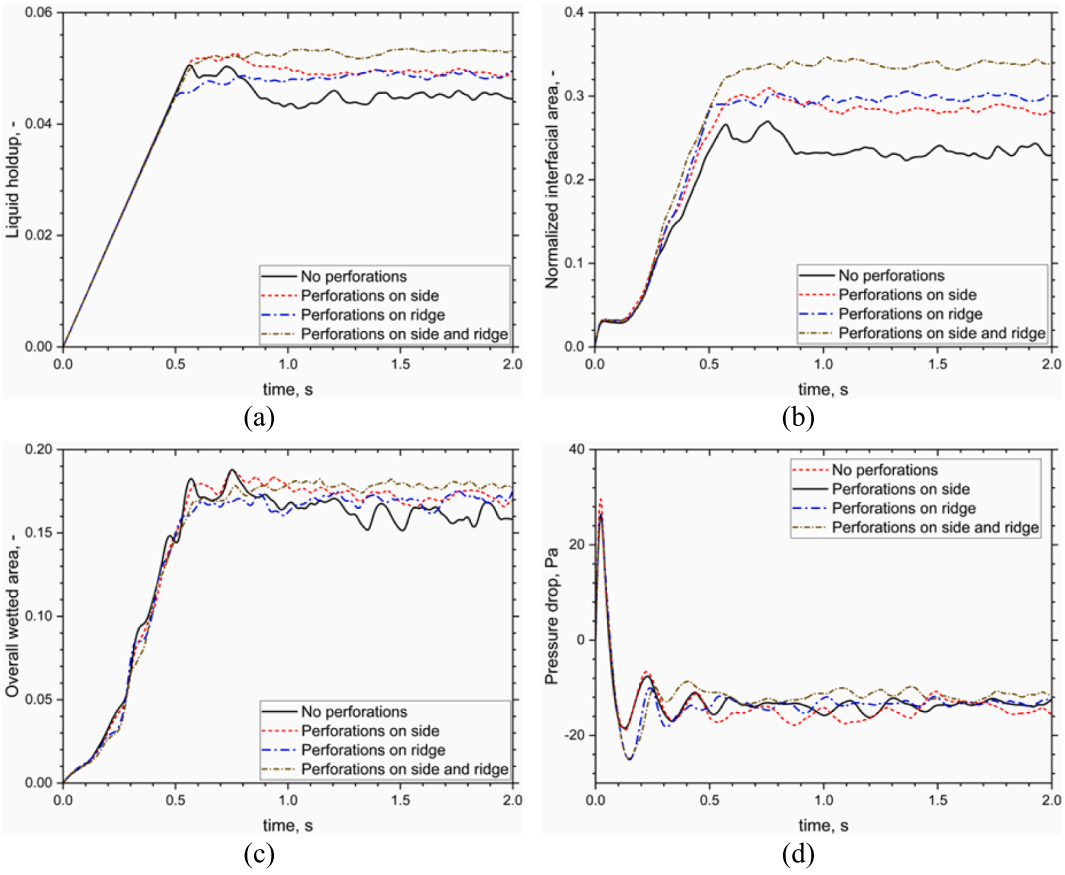


**Fig. 10.** Effect of perforation location on (a) liquid holdup, (b) interfacial area, (c) wetted area, and (d) pressure drop ($\beta = 90^\circ$, $\theta_w = 70^\circ$, $U_l = 62$ m$^3$/m$^2$hr).

Video V1, the flow behavior at a $\beta$ of 90° and $U_l$ of 62 m$^3$/m$^2$hr is unsteady and is associated with droplet formation due to interaction of the liquid-phase with the proximity regions between the two consecutive non-perforated corrugated sheets and the gravity driven nature of the flow. Therefore, for the ease of visualizing the flow path as a function of $U_l$, the time-averaged liquid distribution on the individual sheets is analyzed. As mentioned in Section 3.1, the flow behavior on all the sides of the sheets is similar at a $\beta$ of 90° resulting in identical values of WA. The time-averaged liquid distribution on the right side of Sheet 1 is shown in Fig. 11 as a representative of the flow behavior on all the sides of the sheets as function of $U_l$. As discussed in previous section, at a $U_l$ of 62 m$^3$/m$^2$hr, rivulets are formed near the inlet that follow the flow direction. These rivulets interact with the proximity regions resulting in flow separation i.e. formation of two liquid streams. One of the liquid streams follows the flow direction whereas, the other follows the corrugation. This flow behavior can be visualized from the red colored regions of the time-averaged liquid distribution shown in Fig. 11(b) (i). Further interaction of the newly formed streams with the proximity regions and the gravity driven nature of the flow results in the droplet formation. The regions of droplet formation can be qualitatively identified by values of time-averaged $\alpha_l$ ($\overline{\alpha}_l$) between 0 and 0.5. The dead zones i.e. the zones which do not interact with the liquid-phase at any given time, can be identified by an $\overline{\alpha}_l$ of 0 and are colored blue in Fig. 11.

At a $U_l$ of 31 m$^3$/m$^2$hr, the flow behavior, at the beginning, is very similar to the flow behavior at a $U_l$ of 62 m$^3$/m$^2$hr, wherein rivulet formation, followed by flow separation and droplet formation is visible (see Supplementary Video V5). However, once the flow is established, the liquid-phase flows through the corrugation with little interaction with the proximity regions like the channel flow behavior observed at a $\beta$ of 45° [see Fig. 11(a) (i)]. Such a channel flow behavior is also observed by other researchers at similar conditions [16,24,27]. This flow behavior results in a decrease in the flow metrics in terms of LH, IA, and overall WA as compared to that at a $U_l$ of 62 m$^3$/m$^2$hr [Fig. 12(a)–(c)]. The presence of perforations leads to flow separation and droplet formations. Flow separation as well as droplet formation events result in an increase in IA, as discussed later, and therefore, are desirable for processes governed by fluid–fluid mass transfer. The newly formed liquid streams and droplets not only flow along the corrugation but also along the flow direction [see Supplementary Video V7]. This results in a decrease in the area of dead zones [see Fig. 11(a) (i)–(ii)], which is also evident from the increase in the overall WA in the presences of perforations [see Fig. 12(c)]. Such a flow behavior results in an increase in LH as well as IA. Interestingly, the value of IA at 31 m$^3$/m$^2$hr with perforations resolved is identical to the value of IA at 62 m$^3$/m$^2$hr without perforations resolved [Fig. 12(b)]. Thus, the presence of perforation is equivalent to increasing the liquid load by a factor of 2.

The flow behavior at a $U_l$ of 110 m$^3$/m$^2$hr is very similar to the flow behavior at a $U_l$ of 62 m$^3$/m$^2$hr from the very beginning. However, it is associated with a larger area of the proximity region interacting with the liquid-phase as compared to that at a $U_l$ of 62 m$^3$/m$^2$hr [Fig. 11(b)–(c) (i)]. This results in a substantial decrease in the area of dead zones [Fig. 11(b)–(c) (i)] and is evident from the substantial increase in the overall WA [Fig. 12(c)]. The decrease in the area of dead zones is also associated with increase in the number of droplets as visualized qualitatively from Fig. 11(c) (i) as well as Supplementary Video V6 and leads to an increase in the IA [see Fig. 12(b)]. The presence of perforations results in a further increase in the frequency of flow separation and droplet formation events [see Supplementary Video V8], as is evident from the fluctuations in $\Delta P$ [Fig. 12(d)] and large values of time-averaged shear stress [Supplementary Fig. S10], resulting in a substantial increase in IA [Fig. 12(b)].

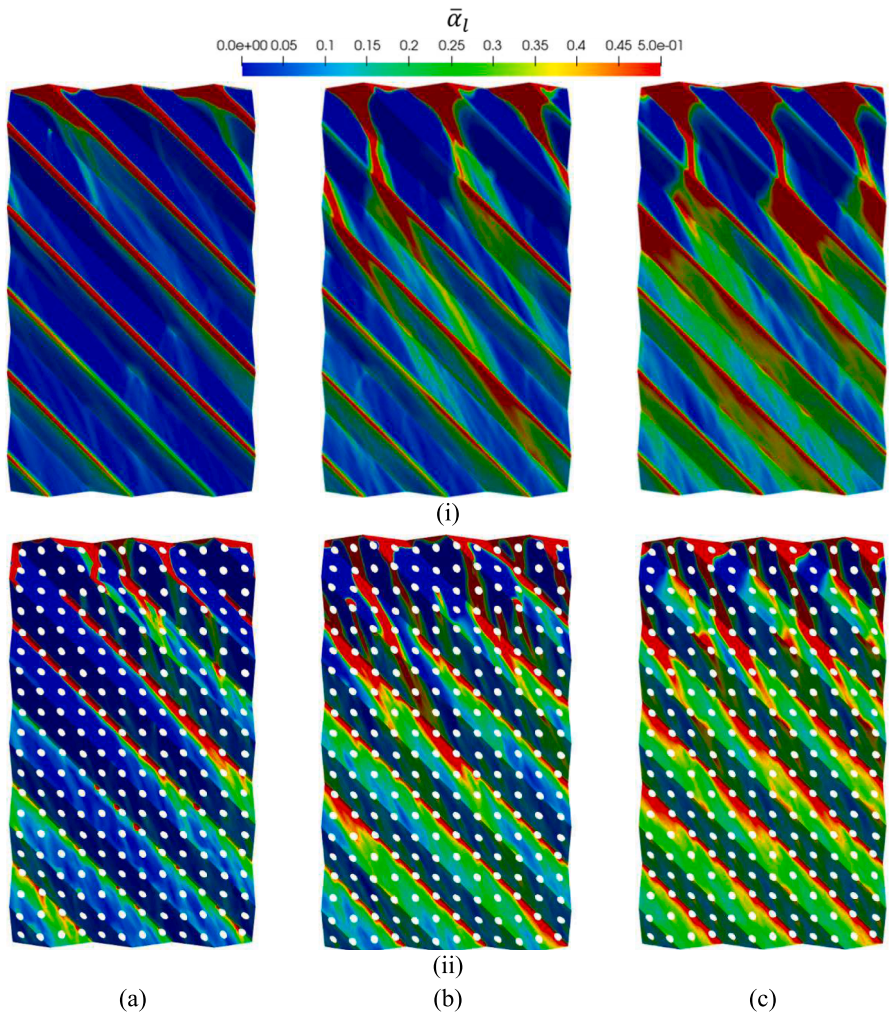


**Fig. 11.** Time-averaged local liquid distribution on the right side of Sheet 2 (i) without and (ii) with perforations at a $U_l$ of (a) 31, (b) 62, and (c) 110 $m^3/m^2hr$. Also see Supplementary Videos V5, V1, and V6 for the time-evolution of liquid distribution on the right side of the non-perforated Sheet 1 at $U_l$ of 31, 62, and 110 $m^3/m^2hr$, respectively. For the dynamics of liquid distribution on the right side of perforated Sheet 1 at $U_l$ of 31, 62, and 110 $m^3/m^2hr$, see Supplementary Videos V7, V4, and V8, respectively ($\beta = 90°$, $\theta_w = 70°$).

### 3.3. Effect of surface wettability

The contact angle, $\theta_w$ was specified to be 70, 50, and 30° to investigate the effect of surface wettability on the flow behavior and hydrodynamic performance of corrugated sheets at a $\beta$ of 90° and a $U_l$ of 62 $m^3/m^2hr$. Investigating the effect of surface wettability is also equivalent to investigating the role of surface textures, as the strategy of considering surface textures through effective/apparent $\theta_w$ is widely accepted[7,9,15,16,24,26]. Further, the fine grid resolution with 6 million elements was required to resolve local flow through non-perforated sheets at a $\theta_w$ of 30° unlike the medium grid resolution with 1.8 million elements at a $\theta_w$ of 70°. Therefore, the fine grid resolution was also used for the case with $\theta_w$ of 50°. Moreover, the fine grid resolution was also used to spatially discretize domains with perforations for $\theta_w$ values of 50 and 30° and resulted in 14 million elements.

Fig. 13(i) compares the time-averaged local liquid distribution on the right side of Sheet 1 at different wetting conditions. As discussed earlier, the dynamics of local liquid distribution and the resulting WA is similar irrespective of the side of the individual sheet at $\beta$ of 90°. Therefore, the local liquid distribution on the right side of Sheet 1 is shown as a representative of all the sheets. As discussed earlier, at a $\theta_w$ of 70°, rivulets are formed near the inlet. These rivulets interact with the proximity region leading to flow separation. The newly formed liquid streams flow in two different directions and the stream flowing along the flow direction further interacts with the proximity regions downstream leading to droplet formation [see Supplementary Video V1 and Fig. 13 (i) (a)]. The change in $\theta_w$ to 50° results in a similar flow behavior near the inlet and is characterized by flow separation in the proximity region near the inlet similar to that at a $\theta_w$ to 70°. However, it is also associated with the tendency of the liquid-phase to spread over the corrugated sheet [see Fig. 13 (i) (b) and Supplementary Video V9].

The tendency of the liquid to spread over the corrugated sheets resists the formation of droplets in the following interaction with the proximity region. Thus, the interaction of the newly formed liquid streams with the downstream proximity regions not only leads to droplet formation but also results in flow separation, unlike just the droplet formation at a $\theta_w$ to 70°. Such a flow behavior results in a better connectivity of the liquid streams, as evident from Fig. 13 (b) (i). Further decrease in $\theta_w$ to 30° results in an increase in the tendency of the liquid to spread and a proportionate decrease in the droplet formation events as evident from the highly connected local liquid distribution on the corrugated sheets [see Fig. 13 (c) (i) and Supplementary Video V10]. Thus, the decrease in $\theta_w$ from 70 to 30° results in the transition of flow behavior from droplet formation towards full film flow as evident from the increase in the area of red region in Fig. 13 (i). Such film flow behavior at small values of $\theta_w$ is also observed by Gu et al. [15], and Singh et al. [24].

The aforementioned transition from droplet flow towards full film

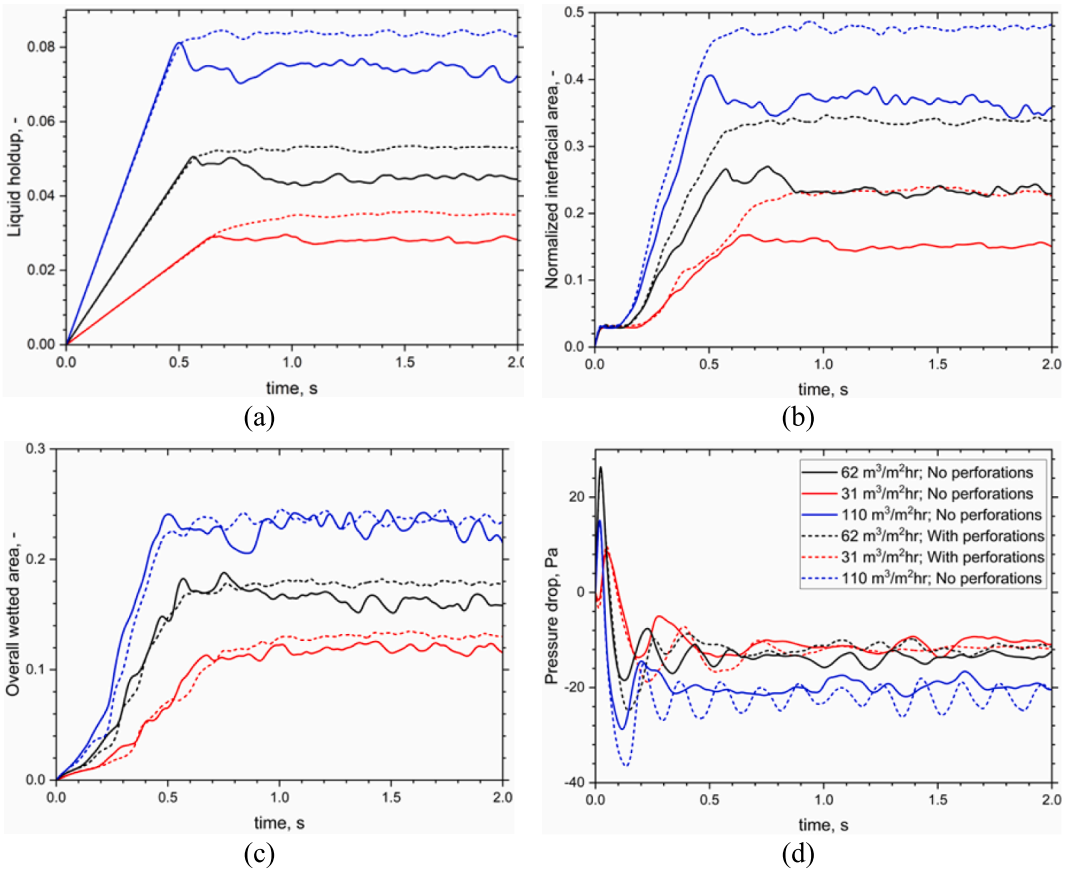


**Fig. 12.** Effect of $U_l$ on (a) liquid holdup, (b) interfacial area, (c) overall wetted area, and (d) pressure drop ($\beta = 90°$, $\theta_w = 70°$).

flow leads to a substantial increase in the LH, IA, and WA with marginal influence on $\Delta P$ [see Fig. 14 (a)–(d)]. This transition is also associated with an increase in the time-averaged wall shear stress because of the increased interaction between the liquid and the corrugated sheet [see Supplementary Fig. S11]. The presence of perforations results in further flow separation as well as droplet formation [see Fig. 13 (ii) and Supplementary Videos V4, V11, and V12] like that observed at other conditions. This leads to a decrease in the area of dead zones irrespective of the surface wettability [see Fig. 13 (ii)]. Therefore, the presence of perforations results in small increases in LH and WA with a substantial increase in IA irrespective of the wetting conditions [see Fig. 14].

In the present work, the liquid-phase is assigned with properties of water. However, in the industry, amines are widely used for $CO_2$ scrubbing from flue gases. Although the density and surface tension of amines are similar to water, their viscosity is substantially larger ($\cong$ 4 to 10 times that of water). Hence, it is also worthwhile to investigate the role of viscosity on the local flow behavior and to ascertain the influence of perforations on the flow metrics of structured packing with high viscosity liquids. Therefore, we varied the viscosity of the liquid from 1 to 16 cP without varying other physical properties and simulated the flow through structured packing with and without perforations resolved. Interestingly, the increase in viscosity has a similar influence on the flow metrics as that of the decrease in $\theta_w$ and the presence of perforations result in an increase in LH, IA, and WA [see Supplementary Fig. S12].

Moreover, in this work, the gas-phase is assumed stagnant whereas in the industry the gas and the liquid phase flow counter-currently with a specific superficial velocity. Consequently, it is also important to comprehend the role of gas-load [$F_G = U_g\sqrt{\rho_g}$, where $U_g$ is the superficial gas velocity at the inlet] on the flow metrics. To understand the role of $F_G$ in counter-current flow situations, we modified the existing domain such that the gas and liquid can be injected simultaneously from the bottom and the top of the fluid domain, respectively. The modified fluid domain with perforations resolved is shown in Supplementary Fig. S13 (a). Further, $F_G$ was varied from 0 to 1 $Pa^{0.5}$ at a constant $U_l$ of 62 $m^3/m^2hr$. The increase in $F_G$ from 0 to 1 $Pa^{0.5}$ had a marginal influence on LH, IA as well as overall WA [see Supplementary Figs. S13 (b)-(d)]. The increase in $F_G$ only resulted in an increase in the pressure drop [see Supplementary Fig. S13 (e)]. Similar observations were reported in recent work by Singh et al. [12] with N-(2-ethoxyethyl)-3-morpholinopropan-1-amine and air as the liquid and gas phase flowing in counter-current way through Schwarz-D structured packing for $F_G < 1$. Structure-resolved counter-current gas–liquid flow simulations for $F_G > 1$ are computationally very demanding, making them beyond the scope of the current study. The above discussion also reveals that the results presented in the previous sections,with $F_G = 0$, are equally valid for $F_G < 1$.

### 3.4. Comparison with correlations in the literature

In this section, we compare LH and IA predicted by structure-resolved VOF simulations with that estimated by some of the correlations available in open literature at a $\beta$ of 90°. At a $\beta$ of 45° the predictions of VOF simulations are not compared with the correlations owing to the availability of limited data points. The comparison as a function of $U_l$ and $\mu_l$ is shown in the Appendix A Fig. A1 and Supplementary Fig. S14, respectively. It is evident from these figures that both LH and IA are underpredicted by the structure-resolved VOF simulations as compared to the correlations other than that by Singh et al. [24]. Most of these correlations are semi-empirical and are proposed based on the bed scale measurements performed with a certain structured packing as well as at specific conditions [36–41]. Therefore, these correlations do not consider $\theta_w$ or surface textures of the corrugated sheets as a variable.

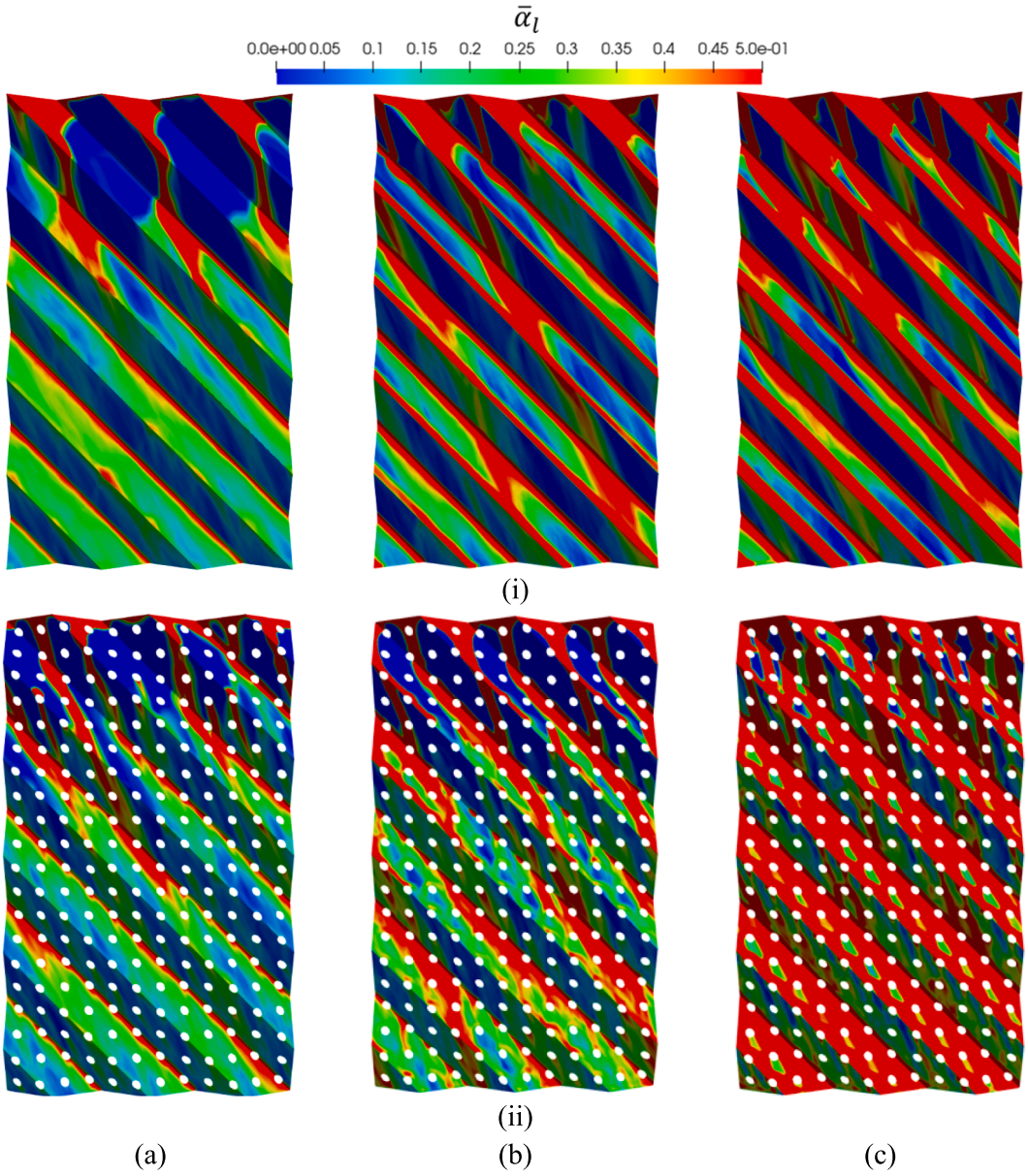


**Fig. 13.** Time-averaged local liquid distribution on the right side of Sheet 1 (i) without and (ii) with perforations at a $\theta_w$ of (a) 70, (b) 50, and (c) 30°. Also see Supplementary Videos V1, V9, and V10 for the time-evolution of liquid distribution on the right side of the non-perforated Sheet 1 at a $\theta_w$ of 70, 50, and 30°, respectively. For the dynamics of liquid distribution on the right side of perforated Sheet 1 at a $\theta_w$ of 70, 50, and 30°, see Supplementary Videos V4, V11, and V12, respectively ($\beta = 90°$, $U_l = 62$ m$^3$/m$^2$hr).

In Section 3.3, we show that $\theta_w$ significantly influence the local liquid distribution and the resulting flow metrics, in terms of LH, IA, and WA. Similar relationship between $\theta_w$ and flow metrics is reported by Singh et al. [24] using structure-resolved VOF simulations of Gemapak-3A, which motivated them to propose correlations considering $\theta_w$ as a variable. However, Singh et al. [24] performed structure-resolved simulations without resolving the perforations on Gemapak-3A. Since the geometric specifications of Mellapak.250 are similar to that of Gemapak-3A, the predictions of structure-resolved simulations without resolving perforations reported here are in agreement with the correlations proposed by Singh et al. [24] [see Fig. 15].

Since the industrially used structured packings are often perforated, further work is required to improve the correlations by Singh et al. [24] (such that the role of perforations is considered) as evident from Fig. 15. Moreover, the LH correlation by Singh et al. [24] significantly over estimate's LH with increasing $\mu_l$ and needs corrections [see Fig. S14 (a) (i)]. Overall, since the corrugated sheets used in the industry are textured as well as perforated the predictions of structure-resolved VOF simulations with $\theta_w$ approaching 0° and perforations resolved are in a relatively better agreement with the correlations [see Appendix A Figs. A1 (b) (i) and (ii)].

## 4. Summary and conclusions

In the present work, periodic sections of perforated and non-perforated structured packing with corrugated sheet specifications corresponding to Sulzer Mellapak.250 are created. The gas–liquid hydrodynamics through structure-resolved fluid domains of the periodic sections is simulated using the VOF method implemented in the open-source C++ library OpenFOAM v6. The role of perforations and their locations at an inclination angle of 45 and 90° on the dynamics of local liquid distribution and the resulting flow metrics is investigated. We show that at a $\beta$ of 45°, the local liquid distribution on the bottom side of sheets is substantially influenced by the location of perforation. The

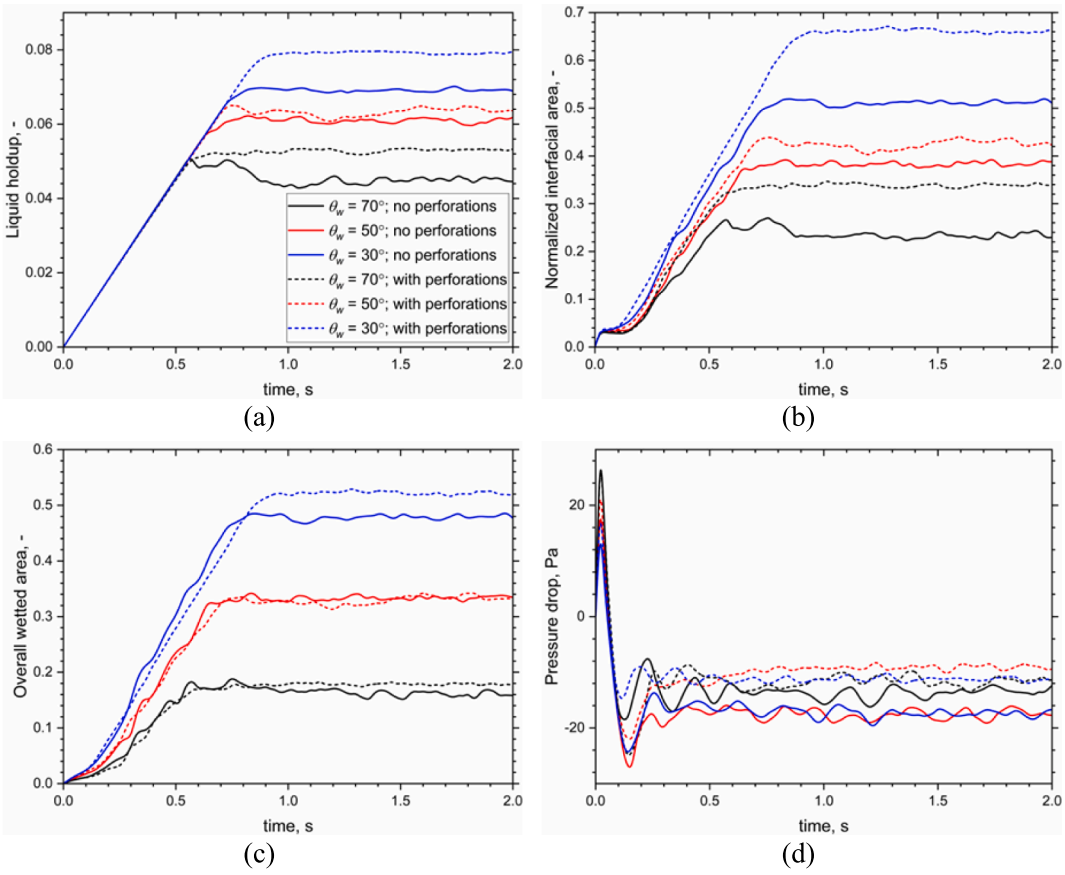


**Fig. 14.** Effect of surface wettability on (a) liquid holdup, (b) interfacial area, (c) overall wetted area, and (d) pressure drop ($\beta = 90°$, $U_l = 62$ m$^3$/m$^2$hr).

presence of perforations on the side leads to droplet flow whereas, the presence of perforation on the ridge results in newly formed liquid streams flowing along the corrugation of the bottom side. Since the majority of liquid flows through the channel provided by the corrugations on the top side, the flow behavior for perforation located on the ridge and on both ridge and side is similar with a small redistribution of liquid. This also results in a substantial increase in LH, WA, and IA relative to the non-perforated sheets.

At a $\beta$ of 90°, small values of $U_l$ result in channel flow in the absence of perforations, whereas at intermediate and large values of $U_l$, the liquid-phase rivulets interact with the proximity region resulting in flow separation. The newly formed liquid streams break to form droplets due to their interaction with the following proximity regions and the gravity-driven nature of the flow. Such a flow behavior leads to an increase in LH, WA, as well as IA with marginal differences in Δ P. Further, the decrease in $\theta_w$ results in a decrease in the tendency of droplet formation due to the interaction of the liquid phase with the proximity regions. This leads to an increase in the connectivity of the newly formed liquid streams post flow separation at the proximity regions i.e. the local flow behavior transits towards full film flow. This flow behavior results in a decrease in the area of dead zones and a proportionate increase in WA, IA, as well as LH. The presence of perforation promotes flow separation as well as droplet formation and is characterized by large values of local time-averaged wall shear stress, irrespective of their location. Since all the perforations interact with the liquid phase, at some or the other time instance, irrespective of their location, the flow metrics at a $\beta$ of 90°, are governed by the number of perforations. The presence of perforations results in a substantial increase in IA and LH with marginal change in overall WA owing to increased flow separation as well as droplet formation irrespective of $U_l$ and $\theta_w$. These findings provide the following insights into the design decisions for improved flow metrics, with a particular emphasis on interfacial area,

- The inclination angle '$\beta$' of 90° from the horizontal provides the highest interfacial area as relative to the other value of $\beta$ considered in the present work. Therefore, the structured packings are recommended to be used at a $\beta$ of 90°.
- The presence of perforations significantly enhances resulting interfacial area irrespective of the operating conditions. Further, at a $\beta$ of 90°, the location of the perforations marginally influence flow metrics and the flow metrics are governed by the number of perforations. This implies that the interfacial area can be further increased by increasing the number of perforations.
- As mentioned in Section 1, the surface texture of the structured packing is modelled by considering apparent static contact angle '$\theta_w$'. Our findings show that the smaller values of $\theta_w$ correlate with improved performance in terms of interfacial area while exhibiting only a marginal influence on pressure drop. Therefore, surface textures should be designed in such a way that the apparent contact angle approaches 0° as practiced in the industry.

Further, we also compared the predictions of structure-resolved VOF simulations with estimates of some of the correlations in the literature, in terms of LH and IA. The structure-resolved VOF simulations significantly underpredicted both LH and IA at large values of $\theta_w$ relative to the correlation developed based on bed-scale measurements. The agreement of the VOF predictions with the estimates of correlations increased with a decrease in $\theta_w$. We also report a good agreement in the predicted LH and IA, for cases without perforations, with that estimated by the correlations proposed by Singh et al. [24] which considered $\theta_w$ as a variable. We also show that the correlations by Singh et al. [24] underpredicted both LH and IA for cases with perforations, irrespective

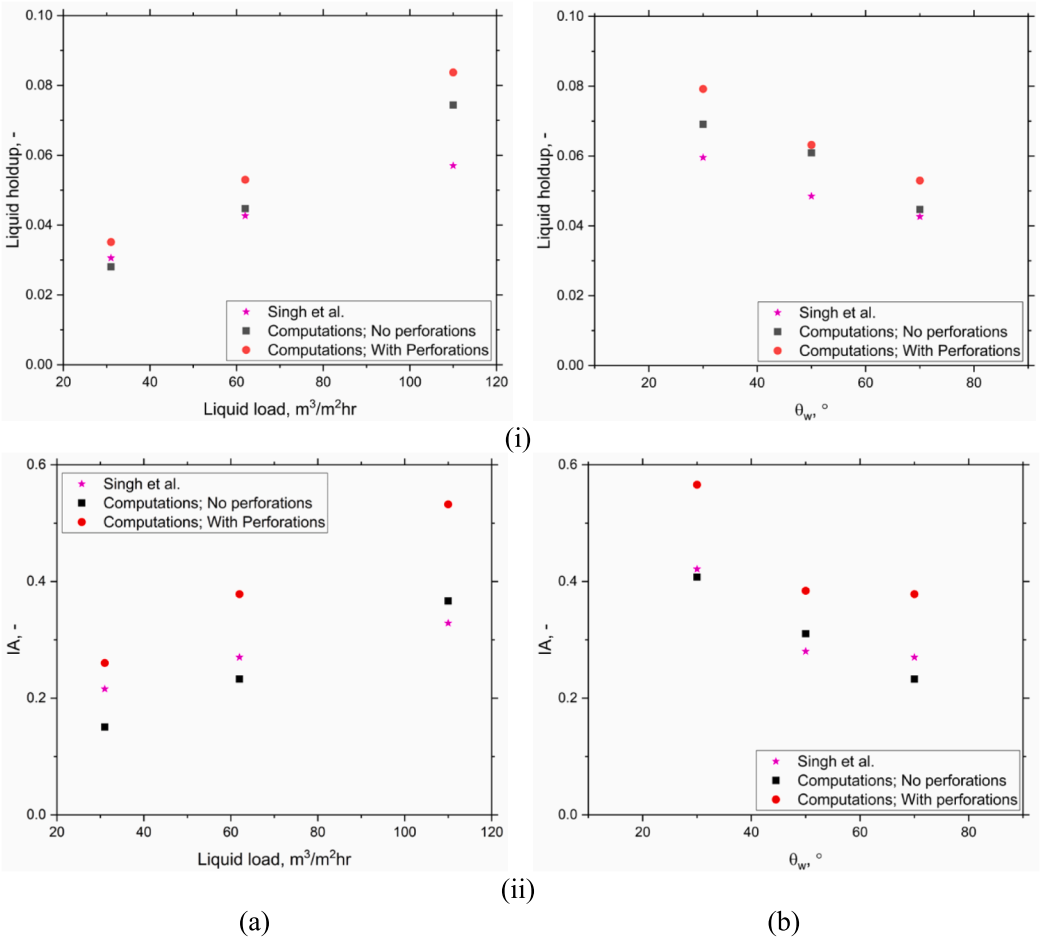


**Fig. 15.** Comparison of computed (i) liquid holdup and (ii) interfacial area with that estimated by the correlations proposed by Singh et al. [24] as a function of (a) $U_l$ at $\theta_w$ of 70° and (b) $\theta_w$ at $U_l$ of 62 $m^3/m^2hr$ ($\beta = 90°$, $\mu_l = 1$ cP).

of $U_l$ as well as $\theta_w$ and require improvements in terms of incorporating the role of perforations. The findings of the present work can also be utilized to propose new correlations and to improve existing correlations used to estimate flow metrics. Additionally, the numerical methodology presented in this work can be utilized to investigate the role of various geometrical characteristics of the structured packings and to design new packings based on the insights from the structure-resolved VOF simulations.

## CRediT authorship contribution statement

**Aniket S. Ambekar:** Conceptualization, Formal analysis, Funding acquisition, Writing – original draft. **E.A.J.F. Peters:** Supervision, Writing – review & editing, Project administration, Funding acquisition. **Olaf Hinrichsen:** Project administration, Writing – review & editing, Supervision. **Vivek V. Buwa:** Writing – review & editing, Supervision. **J. A.M. Kuipers:** Project administration, Writing – review & editing, Resources, Supervision, Funding acquisition.

## Declaration of competing interest

The authors declare that they have no known competing financial interests or personal relationships that could have appeared to influence the work reported in this paper.

## Data availability

Data will be made available on request.

## Acknowledgments

The authors acknowledge the funding received from the European Union's Horizon 2020 research and innovation programme under the Marie Skłodowska-Curie grant agreement no. 899987. The authors are thankful to SURF and IITD for computational and software resources, respectively.

## Appendix

*Appendix A:. Comparison of LH and IA predictions with correlations in the literature*

As mentioned in Section 3.4, we compared the LH and IA predictions of structure-resolved VOF simulations with few of the correlations available in open literature for $\beta = 90°$. Most of the correlations, in open literature, are semi-empirical and are proposed based on the bed scale measurements performed with a certain structured packing as well as at specific conditions [36–41]. Since these correlations were proposed based on bed-scale measurements, the static contact angle '$\theta_w$' is not considered as a variable. The correlation by Singh et al. [24] is the only correlation proposed

based on structure-resolved VOF simulations and is therefore a function of $\theta_w$. However, it is developed based on the simulations where perforations on the corrugated sheets were not resolved. The comparison of computed LH and IA, as a function of $U_l$, with that estimated from various correlations is shown in Fig. A1 (a) and (b), respectively. A detail discussion on this comparison is provided in Section 3.4.

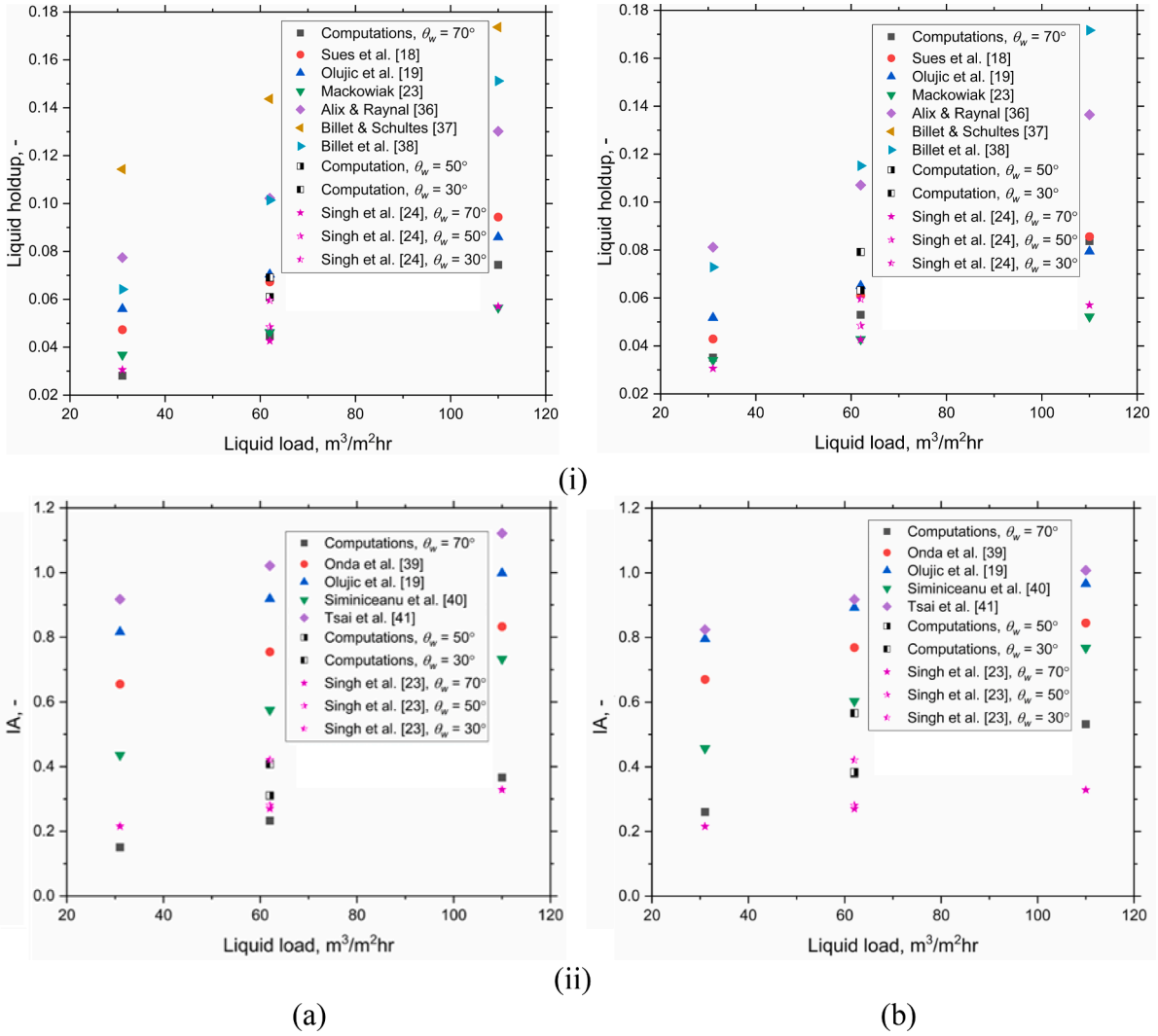


**Fig. A1.** Comparison of computed (i) liquid holdup and (ii) interfacial area with that estimated by the correlations in literature as a function of $U_l$ (a) without and (b) with perforations resolved ($\beta = 90°$, $\mu_l = 1$ cP).

## Appendix B. Supplementary data

Supplementary data to this article can be found online at https://doi.org/10.1016/j.cej.2024.150084.

## References


[1] Y. Amini, M. Nasr Esfahany, CFD simulation of the structured packings: A review, Sep. Sci. Technol. 54 (2019) 2536–2554, https://doi.org/10.1080/01496395.2018.1549078.

[2] M. Schubert, A. Bieberle, F. Barthel, S. Boden, U. Hampel, Advanced tomographic techniques for flow imaging in columns with flow distribution packings, Chem Ing Tech. 83 (2011) 979–991, https://doi.org/10.1002/cite.201100022.

[3] C. Bradtmöller, A. Janzen, M. Crine, D. Toye, E. Kenig, S. Scholl, Influence of Viscosity on Liquid Flow Inside Structured Packings, Ind Eng Chem Res. 54 (2015) 2803–2815, https://doi.org/10.1021/ie502015y.

[4] S. Schug, W. Arlt, Imaging of Fluid Dynamics in a Structured Packing Using X-ray Computed Tomography, Chem Eng Technol. 39 (2016) 1561–1569, https://doi.org/10.1002/ceat.201600278.

[5] S. Flechsig, J. Sohr, M. Schubert, U. Hampel, E.Y. Kenig, A new tomography-based approach for the fluid dynamic description of conventional structured packings and sandwich packings, Chemical Engineering and Processing - Process Intensification. 171 (2022) 108530, https://doi.org/10.1016/j.cep.2021.108530.

[6] Y. Haroun, L. Raynal, P. Alix, Prediction of effective area and liquid hold-up in structured packings by CFD, Chem. Eng. Res. Des. 92 (2014) 2247–2254, https://doi.org/10.1016/j.cherd.2013.12.029.

[7] A. Olenberg, E.Y. Kenig, Numerical investigation of liquid flow morphology in structured packings, Chem Eng Sci. 219 (2020) 115559, https://doi.org/10.1016/j.ces.2020.115559.

[8] A. Hoffmann, I. Ausner, J.U. Repke, G. Wozny, Detailed investigation of multiphase (gas-liquid and gas-liquid-liquid) flow behaviour on inclined plates, Chem. Eng. Res. Des. 84 (2006) 147–154, https://doi.org/10.1205/cherd.05110.

[9] R. Bertling, M. Hack, I. Ausner, B. Horschitz, S. Bernemann, E.Y. Kenig, Modelling film and rivulet flows on microstructured surfaces using CFD methods, Chem Eng Sci. 251 (2022) 117414, https://doi.org/10.1016/j.ces.2021.117414.

[10] H. Lan, J.L. Wegener, B.F. Armaly, J.A. Drallmeier, Developing laminar gravity-driven thin liquid film flow down an inclined plane, Journal of Fluids Engineering, Transactions of the ASME. 132 (2010), https://doi.org/10.1115/1.4002109.

[11] Y. Iso, J. Huang, M. Kato, S. Matsuno, K. Takano, Numerical and experimental study on liquid film flows on packing elements in absorbers for post-combustion CO2 capture, Energy Procedia 37 (2013) 860–868, https://doi.org/10.1016/j.egypro.2013.05.178.

[12] R.K. Singh, Y. Fu, C. Zeng, D.T. Nguyen, P. Roy, J. Bao, Z. Xu, G. Panagakos, Hydrodynamics of countercurrent flow in an additive-manufactured column with

triply periodic minimal surfaces for carbon dioxide capture, Chem. Eng. J. 450 (2022) 138124, https://doi.org/10.1016/j.cej.2022.138124.
[13] L.H. Macfarlan, M.T. Phan, R.B. Eldridge, Structured packing geometry study for liquid-phase mass transfer and hydrodynamic performance using CFD, Chem Eng Sci. 249 (2022) 117353, https://doi.org/10.1016/j.ces.2021.117353.
[14] C.W. Green, J. Farone, J.K. Briley, R.B. Eldridge, R.A. Ketcham, B. Nightingale, Novel application of X-ray computed tomography: Determination of gas/liquid contact area and liquid holdup in structured packing, Ind Eng Chem Res. 46 (2007) 5734–5753, https://doi.org/10.1021/ie0701827.
[15] C. Gu, S. Hu, X. Zhi, S. Zhu, L. Qiu, Numerical analysis of the influence of packing corrugation angle on the flow and mass transfer characteristics of cryogenic distillation, Appl Therm Eng. 214 (2022) 118847, https://doi.org/10.1016/j.applthermaleng.2022.118847.
[16] L. Yang, F. Liu, K. Saito, K. Liu, CFD modeling on hydrodynamic characteristics of multiphase counter-current flow in a structured packed bed for post-combustion CO2 capture, Energies 11 (2018) 3103, https://doi.org/10.3390/en11113103.
[17] D. Sebastia-Saez, S. Gu, P. Ranganathan, K. Papadikis, Meso-scale CFD study of the pressure drop, liquid hold-up, interfacial area and mass transfer in structured packing materials, Int. J. Greenhouse Gas Control 42 (2015) 388–399, https://doi.org/10.1016/j.ijggc.2015.08.016.
[18] P. Sues, L., Spiegel Sulzer, Hold-up of Mellapak structured packings, Chem. Eng. Process. 31 (1992) 119–124.
[19] Ž. Olujić, A.B. Kamerbeek, J. De Graauw, A corrugation geometry based model for efficiency of structured distillation packing, Chem. Eng. Process. 38 (1999) 683–695.
[20] Ž. Olujić, M. Behrens, L. Colli, A. Paglianti, Predicting the efficiency of corrugated sheet structured packings with large specific surface area, Chem. Biochem. Eng. Q. 18 (2004) 89–96.
[21] R. Billet, M. Schultes, Modelling of pressure drop in packed columns, Chem Eng Technol. 14 (1991) 89–95, https://doi.org/10.1002/ceat.270140203.
[22] J. Stichlmair, J.L. Bravo, J.R. Fair, General model for prediction of pressure drop and capacity of countercurrent gas/liquid packed columns, Gas Sep. Purif. 3 (1989) 19–28.
[23] J.M. Máckowiak, Fluid dynamics of packed columns. Chemische Technik. Verfahrenstechnik. Springer-Verlag Berlin Heidelberg (2010).
[24] R.K. Singh, J.E. Galvin, X. Sun, Multiphase flow studies for microscale hydrodynamics in the structured packed column, Chem. Eng. J. 353 (2018) 949–963, https://doi.org/10.1016/j.cej.2018.07.067.
[25] A. Ataki, H.J. Bart, Experimental and CFD simulation study for the wetting of a structured packing element with liquids, Chem Eng Technol. 29 (2006) 336–347, https://doi.org/10.1002/ceat.200500302.
[26] R.K. Singh, J.E. Galvin, X. Sun, Hydrodynamics of the rivulet flow over corrugated sheet used in structured packings, Int. J. Greenhouse Gas Control 64 (2017) 87–98, https://doi.org/10.1016/j.ijggc.2017.07.005.
[27] R.K. Singh, J. Bao, C. Wang, Y. Fu, Z. Xu, Hydrodynamics of countercurrent flows in a structured packed column: Effects of initial wetting and dynamic contact angle, Chem. Eng. J. 398 (2020) 125548, https://doi.org/10.1016/j.cej.2020.125548.
[28] L. Raynal, A. Royon-Lebeaud, A multi-scale approach for CFD calculations of gas-liquid flow within large size column equipped with structured packing, Chem Eng Sci. 62 (2007) 7196–7204, https://doi.org/10.1016/j.ces.2007.08.010.
[29] J. Fernandes, P.F. Lisboa, P.C. Simões, J.P.B. Mota, E. Saatdjian, Application of CFD in the study of supercritical fluid extraction with structured packing: Wet pressure drop calculations, J. Supercrit. Fluids 50 (2009) 61–68, https://doi.org/10.1016/j.supflu.2009.04.009.
[30] N. Sarajlic, J. Neukäufer, M.A. Ashour, T. Grützner, S. Meinicke, C. Knösche, J. Paschold, H. Klein, S. Rehfeldt, Simulation of the liquid flow distribution in laboratory-scale additively manufactured packings, Chem. Eng. Res. Des. 196 (2023) 28-39, https://doi.org/10.1016/j.cherd.2023.06.035.
[31] J. Huang, M. Li, Z. Sun, M. Gong, J. Wu, Hydrodynamics of layered wire gauze packing, Ind Eng Chem Res. 54 (2015) 4871–4878, https://doi.org/10.1021/ie504689s.
[32] B.D. Hirt, C W and Nicolas, Volume of Fluid (VOF) Method for the Dynamics of Free Boundaries, Jouranal of Computational, Physics 225 (1981) 201–225, https://doi.org/10.1016/0021-9991(81)90145-5.
[33] M. Nekouei, S.A. Vanapalli, Volume-of-fluid simulations in microfluidic T-junction devices: Influence of viscosity ratio on droplet size, Phys. Fluids 29 (2017), https://doi.org/10.1063/1.4978801.
[34] C.J. Greenshields, OpenFoam user guide. Version 6, OpenFOAM Foundation Ltd July, (2017).
[35] C. Brackbill, J.U. Kothe, D.B. Zemach, A Continuum Method for Modeling Surface Tension, Jouranal of Computational, Physics (1992) 335–354, https://doi.org/10.1016/0021-9991(92)90240-Y.
[36] P. Alix, L. Raynal, Liquid distribution and liquid hold-up in modern high capacity packings, Chem. Eng. Res. Des. 86 (6) (2008) 585–591, https://doi.org/10.1016/j.cherd.2008.02.021.
[37] R. Billet, M. Schultes, Predicting mass transfer in packed columns, Chem. Eng. Technol. 16 (1) (1993) 1–9, https://doi.org/10.1002/ceat.270160102.
[38] R. Billet, Packed Towers, Wernheim, Germany, In Processing and Environmental Technology; Wiley-VCH, 1995.
[39] K. Onda, H. Takeuchi, Y. Okumoto, Gas absorption with chemical reaction in packed columns, J. Chem. Eng. Jpn. 1 (1968) 62–66, https://doi.org/10.1252/jcej.1.62.
[40] I. Siminiceanu, et al., Measuring the effective mass transfer area of a structured packing by a chemical method, Rev. Chim. 59 (2008) 1117–1121.
[41] R.E. Tsai, A.F. Seibert, R.B. Eldridge, G.T. Rochelle, A dimensionless model for predicting the mass-transfer area of structured packing, AIChE J 57 (2011) 1173–1184, https://doi.org/10.1002/aic.12345.